INL/JOU-22-69345-Revision-0

Assessing the interfacial corrosion mechanism of Inconel 617 in chloride molten salt corrosion using multi-modal advanced characterization techniques

December 2022

Trishelle Marie Copeland-Johnson, Daniel J Murray, Guoping Cao, Lingfeng He

INL/JOU-22-69345-Revision-0

Assessing the interfacial corrosion mechanism of Inconel 617 in chloride molten salt corrosion using multi-modal advanced characterization techniques

Trishelle Marie Copeland-Johnson, Daniel J Murray, Guoping Cao, Lingfeng He

December 2022

Idaho National Laboratory
Idaho Falls, Idaho 83415

http://www.inl.gov

Prepared for the
U.S. Department of Energy
Under DOE Idaho Operations Office
Contract DE-AC07-05ID14517

frontiers | Frontiers in Nuclear Engineering

TYPE Original Research
PUBLISHED 05 December 2022
DOI 10.3389/fnuen.2022.1049693

EDITED BY
Karl Whittle,
University of Liverpool, United Kingdom

REVIEWED BY
Gordon James Thorogood,
Australian Nuclear Science and Technology Organisation, Australia
David Abrecht,
Oak Ridge National Laboratory (DOE), United States

*CORRESPONDENCE
Trishelle M. Copeland-Johnson,
Trishelle.copelandjohnson@inl.gov
Guoping Cao,
Guoping.cao@inl.gov

SPECIALTY SECTION
This article was submitted to Nuclear Materials, a section of the journal Frontiers in Nuclear Engineering

RECEIVED 20 September 2022
ACCEPTED 09 November 2022
PUBLISHED 05 December 2022

CITATION
Copeland-Johnson TM, Murray DJ, Cao G and He L (2022), Assessing the interfacial corrosion mechanism of Inconel 617 in chloride molten salt corrosion using multi-modal advanced characterization techniques.
Front. Nucl. Eng. 1:1049693.
doi: 10.3389/fnuen.2022.1049693

Assessing the interfacial corrosion mechanism of Inconel 617 in chloride molten salt corrosion using multi-modal advanced characterization techniques

Trishelle M. Copeland-Johnson[1,2]*, Daniel J. Murray[1], Guoping Cao[3]* and Lingfeng He[1,4]

[1]Characterization and Post Irradiation Examination, Idaho National Laboratory, Idaho Falls, ID, United States, [2]Idaho National Laboratory, Glenn T. Seaborg Institute, Idaho Falls, ID, United States, [3]Department of Pyrochemistry and Molten Salt Systems, Nuclear Science and Technology, Idaho National Laboratory, Idaho Falls, ID, United States, [4]Department of Nuclear Engineering, North Carolina State University, Raleigh, NC, United States

The United States Department of Energy (DOE) has committed to expanding the domestic clean energy portfolio in response to the rising challenges of energy security in the wake of climate change. Accordingly, the construction of a series of Generation IV reactor technologies are being demonstrated, including sodium-cooled, small modular, and molten chloride fast reactors (MCFRs). To date, there are no fully qualified structural materials for constructing MCFRs. A number of commercial structural alloys have been considered for the construction of MCFRs, including alloys from the Inconel and Hastelloy series. Informed qualification of structural materials for the construction of MCFRs in the future can only be ensured by expanding the current fundamental knowledgebase of information pertaining to material performance under environmental stressors relevant to operation of the reactor, including corrosion susceptibility. The purpose of this investigation is to illustrate how a correlative multi-modal electron microscopy characterization approach, including the novel application of focused-ion beam 3D reconstruction capabilities, can elucidate the corrosion mechanism of a candidate structural material Inconel 617 for MCFR in NaCl-$MgCl_2$ eutectic salt at 700°C for 1,000 h. Evidence of intergranular corrosion, Ni and Fe dealloying, and Cr-O enrichment along the grain boundary, which most likely corresponds to Cr_2O_3, is a phenomenon that has been documented in other Ni-based superalloys exposed to chloride molten salt systems. Additional corrosion products, including the formation of insoluble $MgAl_2O_4$, within the porous network produced by the salt attack is a novel observation. In addition, Mo_3Si_5 and τ_2 precipitates are detected in the alloy bulk and are dissolved by the salt. Furthermore, the lack of detection of design γ' precipitates in Inconel 617 after 1,000 h could indicate that the molten salt corrosion mechanism has indirectly induced a phase transformation of Al_2TiNi (τ_2) and $Ni_3(Al,Ti)$ (γ') phase. This investigation provides a comprehensive understanding of molten salt corrosion mechanisms in a complex material system such as a commercial structural alloy for applications in MCFRs.

KEYWORDS

molten salt, chloride, Ni-based superalloys, secondary ion mass spectroscopy, 3D reconstruction, electron microscopy, corrosion

1 Introduction

The United States Department of Energy (DOE) has committed to expanding the domestic clean energy portfolio in response to the rising challenges of energy security in the wake of climate change. Accordingly, the DOE Office of Nuclear Energy is highlighting the need to advance Generation IV nuclear energy technologies through collaborations with industry partners with initiatives such as the Advanced Reactor Development Program (ARDP). The construction of a series of Generation IV reactor technologies are being demonstrated through the ARDP, including sodium-cooled, small modular, and molten chloride fast reactors (MCFRs). To date, there are no fully qualified structural materials for constructing MCFRs. Current regulations with the nuclear power section of the American Society of Mechanical Engineers Boiler and Pressure Vessel Code are for traditional water-cooled reactors and cannot translate to MCFR structural materials. Many commercial structural alloys have been considered for construction of MCFRs, including alloys from the Inconel (Olson et al., 2009; Salinas-Solano et al., 2014; Grégoire et al., 2020; Yang et al., 2020; Lei et al., 2021; Pragnya et al., 2021) and Hastelloy series (Yang et al., 2016; Ye et al., 2016; Ding et al., 2018; Ezell et al., 2020; Knosalla et al., 2020). Informed qualification of structural materials for the construction of MCFRs in the future can only be ensured by expanding the fundamental knowledgebase pertaining to material performance under environmental stressors relevant to operation of the reactor, including corrosion susceptibility.

Elucidating molten salt corrosion susceptibility requires delving further into the corrosion mechanism of MCFR structural materials, expanding on the relationship between alloy composition and microstructure on the kinetics and thermodynamics of the corrosion process. To assess changes in alloy composition and microstructure at a length scale indicative for elucidating the corrosion mechanism, a suite of advanced characterization techniques is needed (Indacochea et al., 2001; Shankar et al., 2013; Salinas-Solano et al., 2014; Vignarooban et al., 2014; Gomez-Vidal and Tirawat, 2016; Liu et al., 2017; Wang et al., 2017; Sun et al., 2018a; Ding et al., 2018; Ding et al., 2019; Jalbuena et al., 2019; Yu et al., 2019; Grégoire et al., 2020; JagadeeswaraRao and Ningshen, 2020; Knosalla et al., 2020; Yang et al., 2020; Bawane et al., 2021; Caldwell et al., 2021; Gill et al., 2021; Patel et al., 2021; Pragnya et al., 2021). More importantly, these characterization techniques need to be employed in a corroborative manner through a multi-modal approach to develop a comprehensive assessment of the corrosion mechanism. Such approaches utilize a combination of scanning electron microscopy (SEM), focused ion beam (FIB), transmission electron microscopy (TEM), and scanning/transmission electron microscopy (S/TEM) techniques in conjunction with other capabilities, primarily on model structural material systems to allow for a controlled environment for witnessing the corrosion phenomena. Gill et al. utilized a combination of SEM, TEM along with electrochemical and synchrotron x-ray absorption spectroscopy (XAS) to elucidate Cr dissolution in Ni-20Cr model alloys exposed to $ZnCl_2$ (Gill et al., 2021). Microstructural information was acquired through SEM analysis, followed by higher-resolution chemical and microstructural analysis of the corrosion-alloy interface with TEM. Electrochemical studies and XAS enabled characterizing changes in the molten salt during the corrosion process, with XAS providing an opportunity for *in situ* analysis as the corrosion process is observed in real-time. Bawane et al. combined a quasi *in situ* TEM analysis with synchrotron nano-tomography to assess chemical and microstructural changes at the onset (<60 s) towards maturity (>2 h) of the corrosion propagation in Ni-20Cr model alloys in KCl-$MgCl_2$ (Bawane et al., 2021). Quasi *in situ* TEM provided a novel perspective for capturing time-sensitive changes at a length scale appropriate for assessing kinetic details of chemical evolution and initial crack propagation; However, given the small sampling volume it is not appropriate for a representative assessment of microstructural changes. In turn, x-ray nanotomography, while limited to lower resolutions (<30 nm), is appropriate for generating a global multi-dimensional visualization of microstructural changes, particularly morphological and porosity evolution as a function of time. Together the two complimentary techniques captured key elements at different stages of the corrosion process to generate a comprehensive assessment. Assessing corrosion mechanisms in commercial alloys presents a more complex endeavor compared to that in model alloy systems (Indacochea et al., 2001; Shankar et al., 2013; Salinas-Solano et al., 2014; Gomez-Vidal and Tirawat, 2016; Zhu et al., 2016; Keny et al., 2019; Yu et al., 2019; Grégoire et al., 2020; Yang et al., 2020; Lei et al., 2021; Pragnya et al., 2021). An excellent example is Xi, et al. analysis of microstructural changes in Hastelloy N in FLiNaK molten salt through a complementary application of x-ray diffraction (XRD), electron probe micro-analyzer, synchrotron scanning transmission x-ray microscopy (TXM), SEM, S/TEM, and XAS (Ye et al., 2016). Each technique provided a distinct perspective of the microstructural evolution. For instance, XRD was employed to document bulk crystalline phases before and after the corrosion, while SEM was utilized to document surface microstructure changes after corrosion. In turn, TEM analysis revealed changes in elemental speciation and distribution at localized sites of interest, and EPMA alongside TXM provided high spatial resolution visuals of elemental and chemical evolution.

The purpose of this investigation is to illustrate how a correlative multi-modal characterization workflow can elucidate the corrosion mechanism, particularly elemental and microstructural evolution, of MCFR structural materials in chloride molten salts. For this study, we assessed Inconel 617 (Alloy 617) that has been exposed to $NaCl-MgCl_2$ eutectic salt at 700°C for 1,000 h using a combination of SEM, FIB, and TEM techniques to aid in development of a proposed mechanism by assessing the corrosion attack from mesoscale down to the nanoscale. SEM/FIB provided a global assessment of changes in the elemental composition, chemical composition, microstructure, and morphology from the surface into the bulk on the order of decades of microns deep. FIB analysis included complementary application of energy-dispersive x-ray spectroscopy (EDS) with time-of-flight secondary ion mass spectroscopy (ToF-SIMS) for elemental and chemical analysis, respectively, to assess diffusion of salt and alloy constituents based on secondary x-ray energy and isotopic signatures. ToF-SIMS validates elemental species detected by EDS that may have proximate characteristic x-ray energies or are outside of the detection capabilities of EDS, such as molecular ions originating from oxygen impurities in the salt (Ghaznavi et al., 2022a). In addition, FIB capabilities also grant novel application of slice-by-slice analysis of the corroded alloy for three-dimensional (3D) reconstruction, documenting the evolution in the microstructure and elemental composition with electron backscatter diffraction (EBSD) and EDS, respectively. 3D reconstruction provides a more immersive analysis of the corrosion attack *versus* two-dimensional studies, including enhanced assessment of intergranular enrichment and depletion (Goldstein et al., 2018). Specific sites identified through SEM/FIB are then assessed with S/TEM analysis for more detailed assessment of changes in elemental composition and crystal phase structure with EDS and selected area electron diffraction (SAED), respectively (Carter and Williams, 2016). This investigation provides a comprehensive understanding of molten salt corrosion mechanisms in a complex material system such as a commercial alloy for applications in MCFRs.

2 Materials and methods

2.1 Corrosion test

Alloy 617 was purchased from Magellan Metals. The corrosion test samples with a dimension of 1 mm by 10 mm by 16 mm were cut from the Alloy 617 plate by electrical discharge machining. The samples were then ground using a series of SiC sand papers and then polished using 9 μm diamond suspensions (Allied High Tech.). A 1.2 mm diameter hole was drilled in the samples for aligning the sample in molten salt during corrosion testing. The Alloy 617 samples were tested in $NaCl-MgCl_2$ eutectic salt, prepared from ultra-dry NaCl and $MgCl_2$ salts, in a 50-ml nickel crucible at 700°C for 1,000 h. About 50 g of $NaCl-MgCl_2$ salt was used. The corrosion test was carried out in a resistance furnace located in an argon atmosphere glovebox with ≤ 0.1 ppm moisture and ≤ 10 ppm oxygen, respectively. After the 1000-h corrosion test, the furnace was shut off and the Alloy 617 sample was cleaned up using deionized water to remove the solidified salt sticking on the sample's surface.

2.2 Scanning electron microscopy/focused ion beam

SEM/FIB characterization provides a global analysis of changes in the morphology of the surface and distribution of elemental species, through EDS, after the corrosion attack from the perspective of the surface and cross-sectioning to traverse into the bulk material. SEM analysis also incorporates 3D reconstruction analysis to provide a novel perspective on the extent of corrosion from the surface of the specimen and ToF-SIMS to validate SEM EDS by mapping the distribution of ionic species. SEM/FIB analysis was performed on a TESCAN Lyra 3 FIB and FEI G4 Helios Hydra Plasma-FIB ("Fibby McFibface"). The TESCAN Lyra 3 FIB is equipped with a gallium-based ion source and high brightness Schottky electron gun, capable of operating at accelerating voltages between 200 to 30 keV and probe current ranges from 2 pA to 200 nA with a 5-axis fully compucentric stage for complex milling procedures. Fibby is capable of high-throughput, high-quality, and statistically relevant 3D characterization; cross sectioning; and micromachining using the next-generation 2.5 μA plasma FIB column, capable of quickly delivering four switchable ion species: Xe, Ar, O, and N. Electron beam resolution at coincident point is 0.6 nm at 15 kV and 1.2 nm at 1 kV. Fibby is also equipped with ToF-SIMS, EDS and EBSD analysis capabilities.

2.3 Transmission electron microscopy

TEM characterization is used to characterize changes in elemental and structural properties at local sites of interest identified during SEM/FIB analysis. TEM characterization techniques included high-resolution EDS analysis and selected area electron diffraction (SAED). TEM analysis was performed on an FEI Talos FX200 TEM ("Christine"), equipped with a new 4 k x 4 k Ceta™ 16 M camera with speed enhancement enabling to record and store 40 full (4 k × 4 k pixels) frames per second (and 320 fps for 512 × 512 pixels). Christine has a point resolution of 0.25 nm and STEM resolution of 0.16 nm,

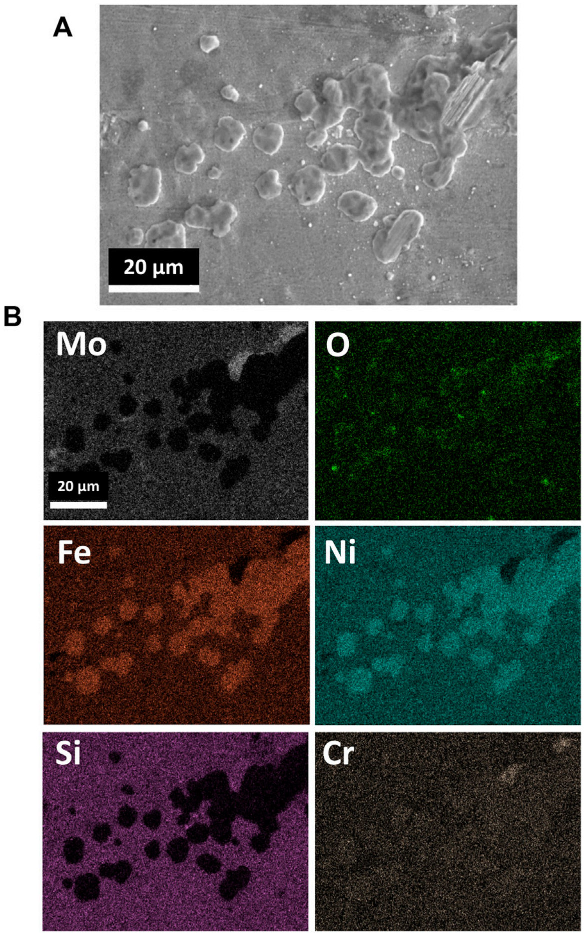

FIGURE 1
SEM images of the **(A)** surface of corroded Alloy 617 alongside **(B)** elemental analysis featuring the distribution of O, Ni, Cr, Mo, Fe, and Si within the region.

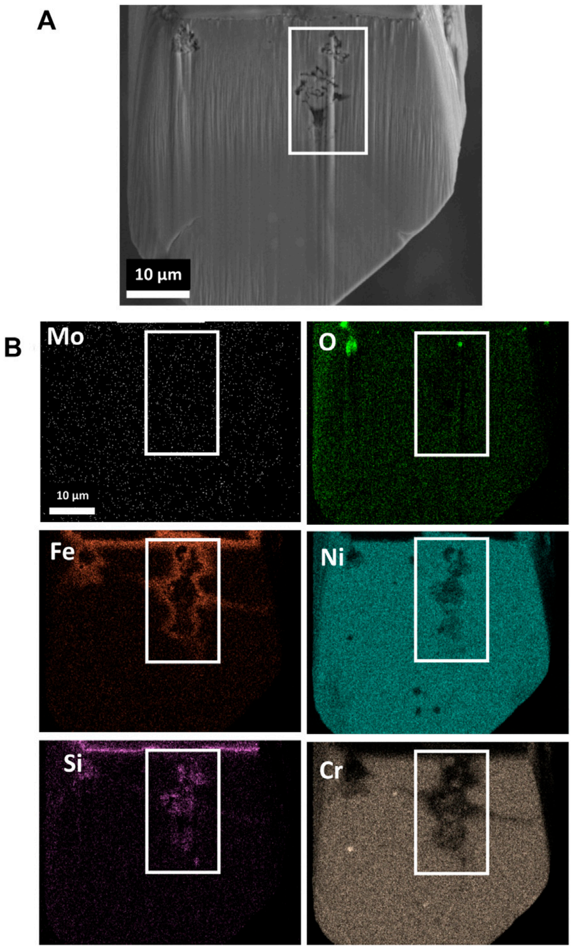

FIGURE 2
SEM imaging of **(A)** cross-sectioned segment of corroded Alloy 617, featuring an example of the porous network developed from the salt attack (bordered in white), alongside **(B)** elemental analysis featuring the distribution of O, Ni, Cr, Mo, Fe, and Si.

equipped with a super-X EDS system with an energy resolution of EDX <136 eV @ Mn Kα for 10 kcps (output counts) at zero-degree sample tilt. Christine is also equipped with an on-axis bright-field/dark-field STEM detector which is composed of a bright-field detector and two dark-field detectors. All detectors are silicon solid-state detectors and can support a beam current up to 3 nA.

3 Results

3.1 Scanning electron microscopy/focused ion beam

3.1.1 Scanning electron microscopy

Analysis of as-received Alloy 617 notes the presence of Mo-, Ti-, and Cr-enriched precipitates distributed throughout the alloy matrix, featured in Supplementary Figure S1. Mo-enriched precipitates were concentrated near grain boundaries. Surface analysis of the corroded Alloy 617, Figure 1, revealed the development of Ni-Fe-enriched globules with respect to the surrounding surface, contributing to an inconsistent, rough morphology over the surface of the material. SEM EDS analysis also cited slight enrichment in Cr and O and depletion of Mo and Si within the globules, with respect to the surrounding area. Traversing into the bulk of the material, Figure 2, reveals that the globules are connected to a porous network, depleted of Cr, Ni, and Fe, with segments of remnant alloy residing within the void structure. Fe enrichment is observed around the porous network and Si enrichment within the porous network, corresponding to the remnant alloy pieces. Finally, highly

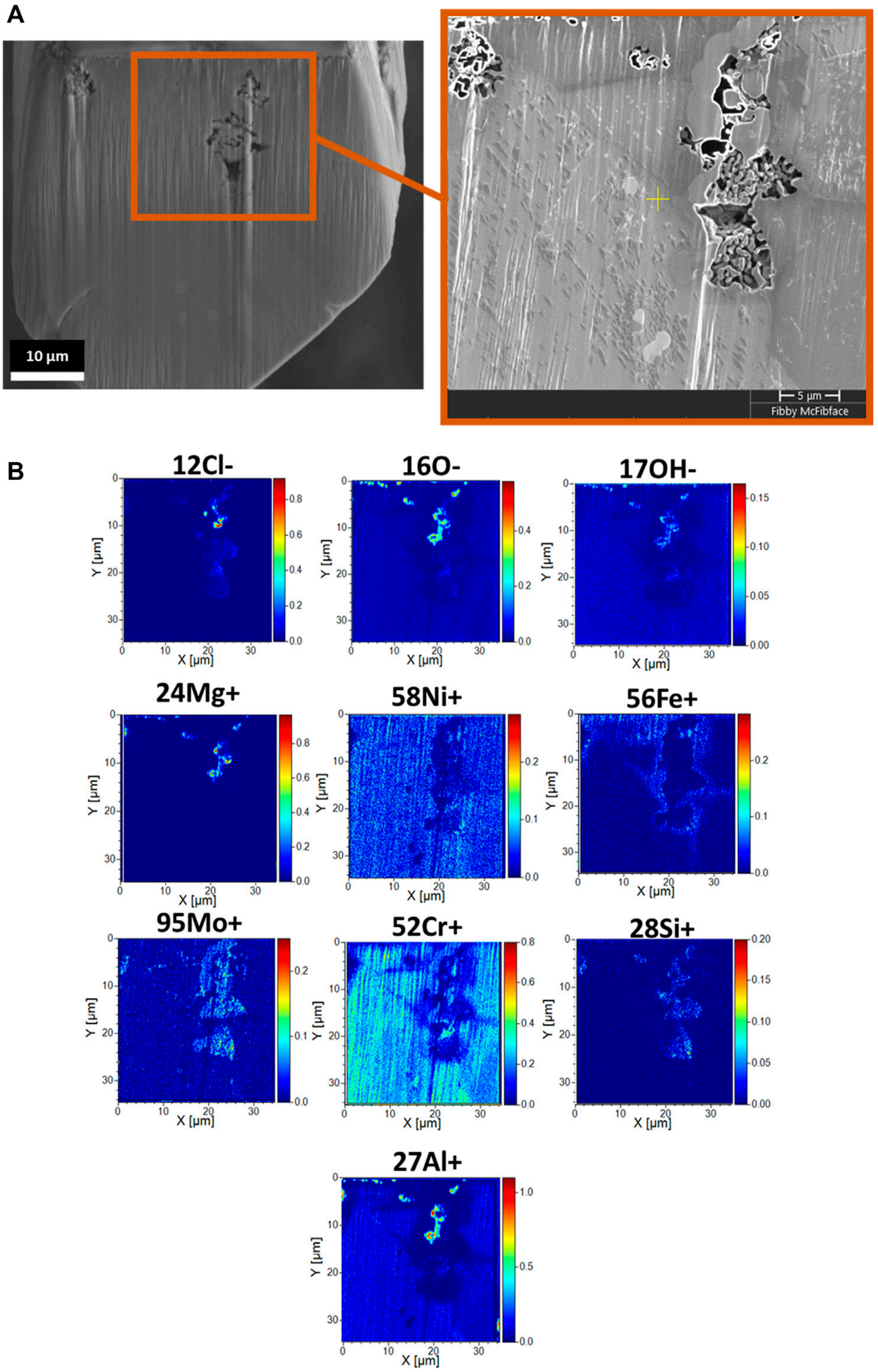

FIGURE 3
ToF-SIMS analysis acquired from **(A)** cross-sectioned segment captured in SEM image featuring an example of a porous network, alongside **(B)** two-dimensional intensity maps illustrating the distribution of ionic species originating from the salt (-Cl, -O, -OH, +Mg) and alloy (+Ni, +Fe, +Mo, +Cr, +Si, +Al).

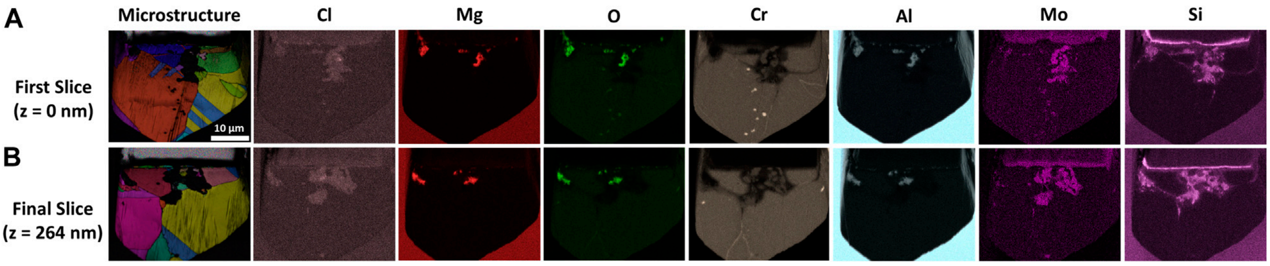

FIGURE 4
Screenshots captured during the **(A)** beginning (z = 0 nm) and **(B)** end (z = 264 nm) of the 3D reconstruction process on corroded Alloy 617, illustrating changes in the microstructure from EBSD analysis and elemental distribution from EDS analysis.

localized O enrichment resides within the porous network with no distinction in the distribution of Mo within and surrounding the porous network.

3.1.2 Time-of-flight secondary ion mass spectroscopy

ToF-SIMS analysis confirms the porous network corresponds to where the salt directly attacked the alloy, based on detection of Cl^- ions within the pores, Figure 3. Additionally, ToF-SIMS corroborates with EDS concerning the depletion of Ni, Cr, and Fe while enrichment of O and Si within the porous network. Enrichment of Fe around the porous network is also in agreement with SEM EDS analysis. ToF-SIMS and EDS signals corresponding to Al and Mg ions are also detected within the porous network, overlapping with the location of O. However, ToF-SIMS provides evidence of Mo enrichment within with porous network, which was not readily detected with SEM EDS analysis. The O- and OH- ion signals were captured from the residual salt within the porous network. It is highly unlikely that the rinsing procedure that removed excess salt from the surface introduced moisture sub-surface to affect the acquisition of the O- and OH- ion, given that the signal resides in pores that still contain residual salt.

3.1.3 3D reconstruction

3D EDS and EBSD reconstruction of a 50 by 70 by 0.264 μm segment of corroded alloy extracted from the bulk specimen captures grain boundary phenomena traversing deeper into the material, Figure 4. 3D EDS analysis reiterates Cr, Ni, and Fe depletion within the porous network. In addition, intergranular Cr-O enrichment is observed along and in localized regions near grain boundaries that are in contact with the porous network, ahead of the corrosion front. Additional evidence of O enrichment is observed within the porous network, overlapping with signals corresponding to Al and Mg. Full animations of the 3D EDS and EBSD reconstruction are available in the data repository.

3.2 Transmission electron microscopy

TEM analysis targets two regions observed in SEM/FIB characterization: 1) a segment of the porous network, featuring residual salt trapped in the pores, and 2) ahead of the corrosion front. The porous network region, Figures 5A, is further analyzed at two specific locales: 1) at the suspected entry point of the attack, Figures 2, 5B) and 2) deeper into the porous network, Figure 5C. A Ni-Fe enriched surface globule observed initially with SEM analysis was captured near the entry point. Overlap of Mg, Al, and O signals and Mo and Si signals are within the entire porous network, in agreement with SEM/FIB analysis. Also, evidence of Cr dissolution is detected by enrichment within a thin region at the entry point of the initiation site, most likely residual material from Cr dissolved into the molten salt. Deeper into the porous network, where residual alloy is present, contained depleted in Cr, Fe, and Ni with respect to the surrounding matrix. SAED analysis, Figure 6, noted two separate grain orientations of the alloy matrix adjacent to the porous network, from the [110] (Figure 6B) to [114] (Figure 6C) zone axis, an indicator of intergranular corrosion. Additional SAED analysis of a Mg-Al-O enriched region within the porous network, Figure 7A, identified $MgAl_2O_4$ shown in Figure 7B along the [001] zone axis. Salt penetration, evidence of the porous network propagating, is observed ahead of the corrosion front, Figure 8, indicated by the presence of Cl signal and Fe enrichment (Figure 8B) with respect to the surrounding matrix. The observation of Fe enrichment is a similar trend that has been observed around the porous network. However, signs of Cr depletion and O enrichment have yet to be detected. Ti-Al-Ni, Mo-Si, and Cr enriched precipitates were present ahead of the corrosion front, in agreement with Mo-, Ti-, and Cr-enriched precipitates detected with SEM/FIB analysis, Supplementary Figure S1. SAED analysis of Mo-Si enriched precipitates are consistent with the presence of Mo_3Si_5, Figure 8C, and Ti-Al-Ni enriched precipitates are consistent with the presence of ternary aluminide intermetallic compound, Al_2TiNi (τ_2 phase), featured in Figure 8C along the [011] zone axis (Huneau et al., 1999; Raghavan, 2005).

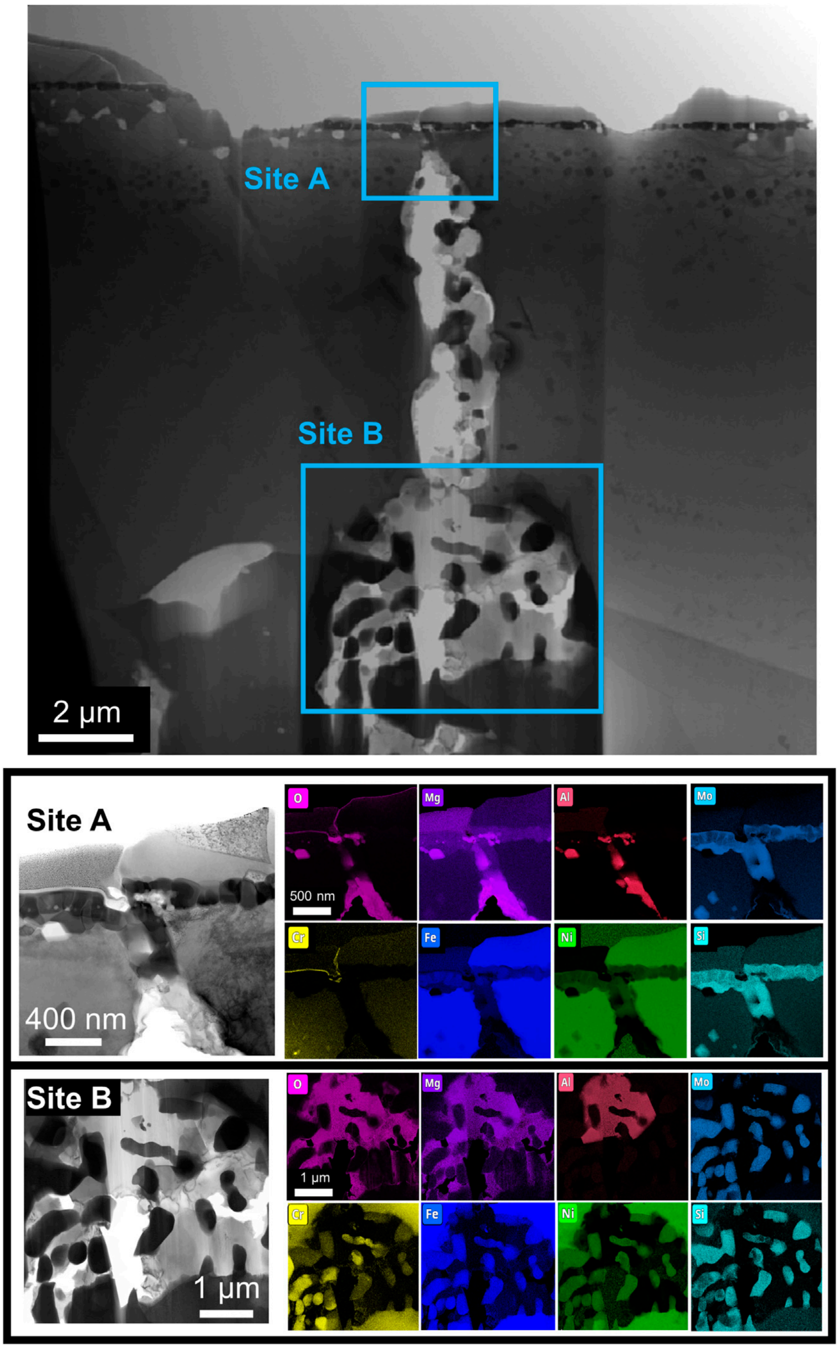

FIGURE 5
(A) Brightfield TEM image of a porous network from corroded Alloy 617, including EDS elemental analysis on two sites of interest **(B)** Site A located near the suspected origin point of the attack and **(C)** Site B deeper in the porous network.

4 Discussion

Multi-modal characterization, utilizing SEM, FIB, and TEM techniques are used to elucidate the corrosion mechanism of Alloy 617 after exposure to NaCl-$MgCl_2$ eutectic salt. The major elements of the corrosion attack include intergranular dealloying at specific grain boundaries, notably Fe, Ni, and Cr, aligned with the formation of Fe-Ni enriched surface globules in proximity to the suspected origin point of the corrosion attack. As a result, a discontinuous porous network forms, featuring insoluble

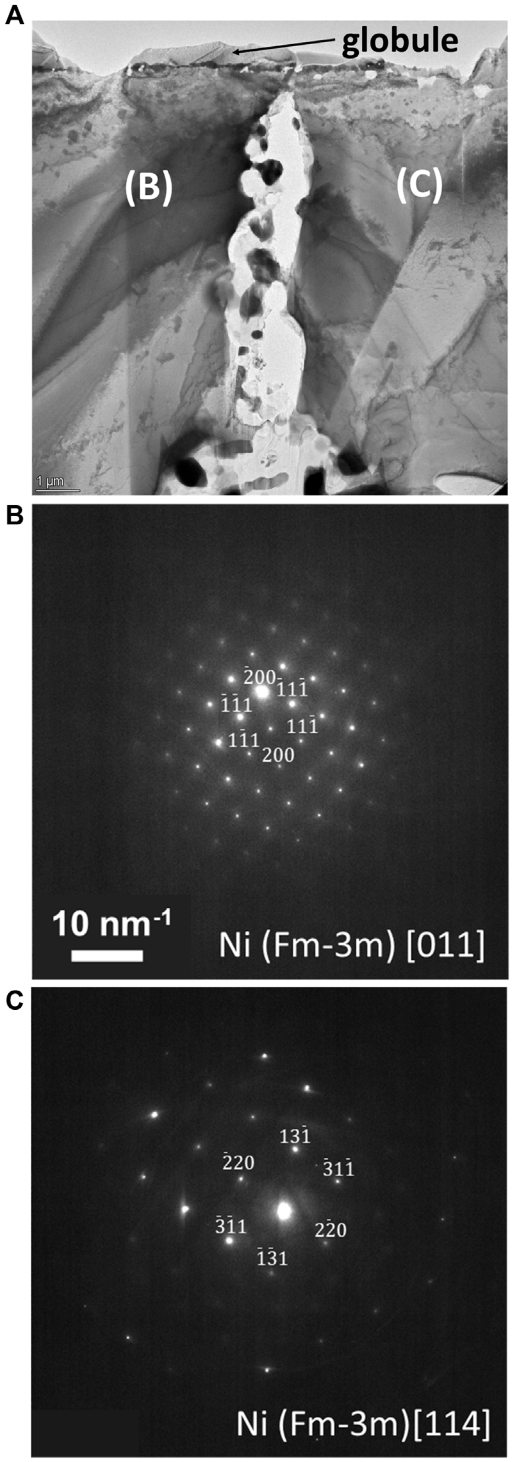

FIGURE 6
(A) Brightfield TEM image of Site A, labeling a surface globule and layer of salt with Mo and Si enrichment and an arrow (in red) noting the point at which the salt is suspected to have begun penetrating into Alloy 617. Comparison of diffraction patterns **(B,C)** captured from the alloy matrix across the entry point. Same scale bar applies to (b) and (c).

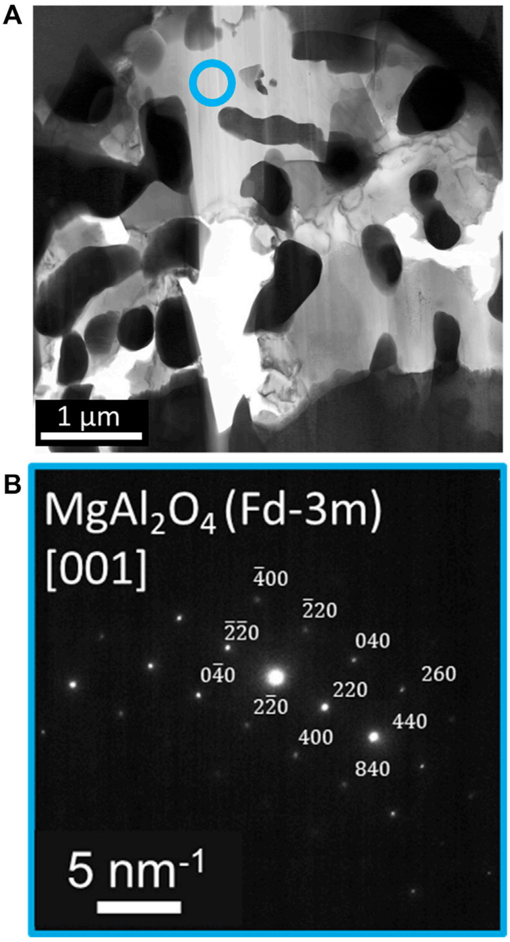

FIGURE 7
(A) Brightfield TEM image of Site B with the acquisition site, circled in blue, where Mg-Al-O enrichment detected from EDS analysis was correlated to **(B)** electron diffraction pattern corresponding to $MgAl_2O_4$.

internal oxidation product, $MgAl_2O_4$, and enveloped in Fe enrichment. Ahead of the corrosion front, evidence of coherent intergranular Cr and O enrichment, Fe enrichment around regions where salt has begun to percolate, and intermetallic τ_2 and Mo_3Si_5 precipitates are observed throughout the entire system. These precipitates presumably dissolve into the salt given the lack of precipitates present in the residual alloy in the porous network.

Intergranular corrosion in Ni-based superalloys, including members of the Inconel family, has been cited by other investigators. This phenomenon is usually coupled with dealloying, particularly Cr (Koger, 1974; Zhu et al., 2016; Guo et al., 2018; Knosalla et al., 2020; Ghaznavi et al., 2022b). For instance, Pragnya et al. analyzed Inconel 625 corroded in $MgCl_2$-NaCl-KCl in a TEM *in situ* environmental cell assembly heated to

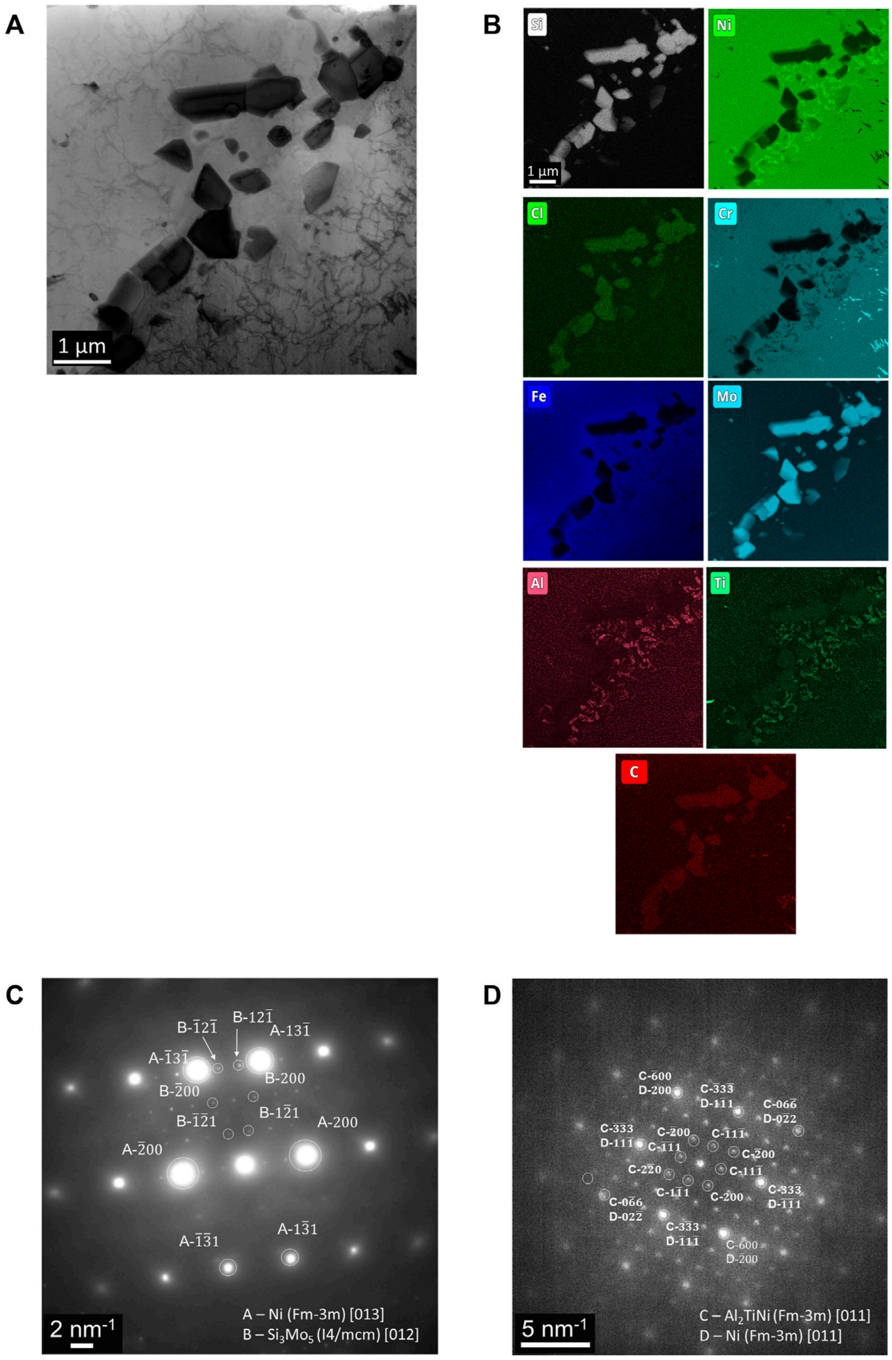

FIGURE 8
(A) Brightfield STEM image featuring Mo-Si-C and Al-Ti-Ni enriched precipitates within the alloy matrix ahead of the corrosion front, **(B)** elemental analysis highlighting enrichment of select elements both originating from the salt and from the alloy, and **(C)** indexed SAED pattern originating from Mo-Si-C and Al-Ti-Ni enriched precipitates corresponding to Mo_3Si_5 and Al_2TiNi, respectively.

700 or 800°C and observed that intergranular corrosion through the material (Pragnya et al., 2021). Knosalla, et al. cited significant intergranular Cr depletion detected in Inconel 617 exposed to a KCl-LiCl eutectic mixture at 800°C for 167 h under Ar (Knosalla et al., 2020). This behavior was documented in this investigation. SEM and TEM EDS analysis detected salt constituents within the porous network, Figure 5, suggesting the salt penetrated the alloy through capillary action (Grégoire et al., 2020). Furthermore, the

discontinuous porous network observed in this study corresponds to intergranular attack, which has been observed in Alloy 617 over shorter time scales (Sun et al., 2018a).

The dealloying of Cr in Alloy 617 due to molten salt corrosion is commonly attributed to the formation of corrosion products, specifically Cr_2O_3, from Cr reacting with oxidant impurities in the salt, such as water (Salinas-Solano et al., 2014; Zhu et al., 2016; Guo et al., 2018; Grégoire et al., 2020; Knosalla et al., 2020; Yang et al., 2020). Several mechanisms explaining the role of Cr in propagating the corrosion front have been proposed. Grégoire et al. characterized Inconel 600 corroded in NaCl-KCl eutectic at 700°C in argon at 20, 100, and 300 h, in which Cr_2O_3 formation and a resulting porous network were observed (Grégoire et al., 2020). Overall, the investigators attributed the formation of the porous network to preferential dissolution of Cr from alloy through micro-galvanic pair development between Cr-based carbides, which are commonly cited during the annealing process, and the remaining alloy matrix. The corrosion mechanism is explained in three steps: 1) intergranular Cr-based carbide precipitate formation due to the significantly larger diffusivity of C in Ni ($\sim 10^{-9}$ cm^2/s) *versus* Cr in Ni ($\sim 10^{-11}$ cm^2/s). 2) establishment of galvanic coupling effect when in direct contact with salt, producing a large electromotive force between the carbide and Ni alloy matrix as anodes and cathodes, respectively. 3) the galvanic coupling effect corresponding to the oxidation of the least noble element, Cr, located within the Cr carbide precipitates, through the reduction of O and Cl to form Cr_2O_3 and $CrCl_2$, respectively. Ultimately, Cr dissolution from the precipitates establishes a concentration gradient towards the surface of the bulk material, coupled with diffusion of C released from the dissolved carbides further into the bulk to form new precipitates, establishing a positive feedback loop that propagates the corrosion front. Intergranular Cr-O enrichment is another postulated mechanism. Zhu et al. explains that the introduction of oxidant impurities, like H_2O, increases the basicity of molten chloride salt, hereby increasing the activity of the oxygen ion, which in turn increases its solubility. As a result, oxygen ions originating from moisture in the salt preferentially react with Cr over Ni, primarily along grain boundaries, which then contribute to the development of the suspected internal oxidation zone (Zhu et al., 2016). As mentioned prior, the detection of OH^- and O^- ion signals by SIMS in residual salt within the porous network is evidence that moisture impurities persist within the chloride salt despite extensive sample preparation in an argon atmosphere. This argument is further supported by the fact that the OH^- and O^- signals detected by ToF-SIMS overlap with Mg^- and Cl-signals corresponding to residual salt trapped within the pores. As noted, Cr_2O_3 has been regularly cited by other investigators (Salinas-Solano et al., 2014; Zhu et al., 2016; Grégoire et al., 2020; Knosalla et al., 2020; Yang et al., 2020). In this investigation, intergranular Cr-O formation is an indicator of Cr_2O_3 formation contributing to the propagation of the corrosion front.

Interestingly, other corrosion products were observed after the corrosion attack. In this investigation, the formation of $MgAl_2O_4$ spinel compound was detected, supported by the detection of Mg-based oxides from other investigators. Zhu et al. exposed Inconel 625 in $NaCl/KCl/MgCl_2/CaCl_2$ mixtures at 900°C for 20 h. Alongside Cr_2O_3, the investigators observed that alloys exposed to KCl-containing mixtures produced NiO, and $NiCr_2O_4$ while in $MgCl_2$-containing mixtures $MgCr_2O_4$, $NiCr_2O_4$, and $NiCrO_3$ were detected (Zhu et al., 2016). Yang et al. corroded Inconel 625 in KCl–$MgCl_2$ for up to 60 h at 700 and 900°C and detected the formation of a MgO scale on the surface of Inconel 625 at 700°C (Yang et al., 2020). Sun et al. also detected MgO subsurface products forming within the voids of the porous network of as early as 100 h (Sun et al., 2018b). In both Sun and Yang's investigations, the distribution of Al was not included, hence there is a possibility that the presence of $MgAl_2O_4$ may not have been detected by these investigators. Reviewing the redox potential of the major alloying elements of Alloy 617 may provide some explanation to why $MgAl_2O_4$ was observed within the porous network. Major alloying elements present in the nominal composition of Alloy 617 in order of relative abundance are as follows: Ni, Cr, Co, Mo, Fe, and Al (Guo et al., 2018). Among these elements, Al is more active than Cr in chloride salts, prompting its dissolution and reaction with Mg ions from the salt and O from moisture impurities to form the spinel compound. In addition, Fe and Ni dealloying can be explained based by comparison of redox potentials in conjunction with Cr dissolution through grain boundaries, given that Cr and Fe are more preferentially dealloyed compared to Ni and Mo (Guo et al., 2018). Kinetically, Cr could also contribute to dealloying of Fe and Ni. Guo et al. attributes Cr dissolution to prompting Kirkendall void formation and consequently the diffusion of the more noble elements, Ni and Fe, to concentrate around the depleted region, explaining Fe enrichment observed around the porous network with respect to the surrounding alloy matrix (Guo et al., 2020). Cr may also be passively enhancing Ni dealloying by the latter element diffusing along the same routes at Cr, since Ni has been cited to preferentially diffuse intergranularly, leading to rapid depletion along grain boundaries (Knosalla et al., 2020; Yang et al., 2020). In turn, Mo and Fe may proliferate additional Cr dissolution, which has been conjectured to enhance Cr dissolution in Hastelloy N exposed to FLiNaK mixture (Fukumoto et al., 2015). Overall, the Cr-O intergranular and Kirkendall void formation mechanisms are the most plausible based on the results collected from this investigation, but additional study is needed to confirm.

Structures like the Ni and Fe-enriched surface globules observed in this investigation have been observed by others

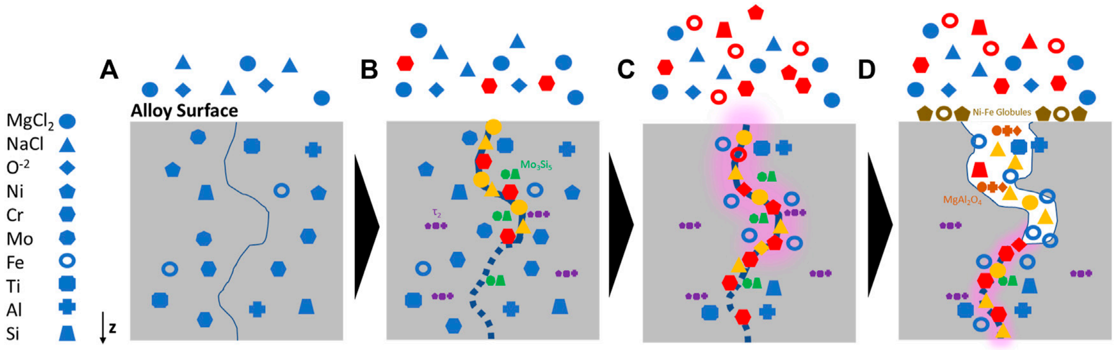

FIGURE 9
Schematic of proposed corrosion mechanism for **(A)** Alloy 617 exposed to NaCl-MgCl$_2$ eutectic salt at 700°C for 1000 h to **(B)** intergranular penetration of the salt constituents (yellow) and subsequent dealloying of Cr (red). During the corrosion process, Mo-enriched precipitates, primarily in proximity to grain boundaries, react with Si to form Mo$_3$Si$_5$ precipitates (green) and Ti-enriched precipitates react with Al and Ni to form τ_2. As the dealloying continued, **(C)** Fe atoms diffuse towards the depletion region (red) and Mo$_3$Si$_5$ and τ_2 precipitates in proximity to the corrosion regime are also dissolved as the porous network develops (highlighted in pink), **(D)** Finally, Mg ions react with Al and O to form MgAl$_2$O$_4$ within the porous network, alongside residual alloying elements and salt as the corrosion propagates further along the grain boundary.

(Zhu et al., 2016; Sun et al., 2018a; Grégoire et al., 2020; Ghaznavi et al., 2022b). Ghaznavi et al. observed similar globular formations in FeNi model alloys after exposure to LiCl-KCl-MgCl$_2$ eutectic at 350°C for 4,000 s but only when the Ni content was above 68 at%, which is well above the maximum threshold for Ni in a nominal composition of Alloy 617 (Limiting Compositions of Alloy, 2019; Ghaznavi et al., 2022b). Sun et al. noted the globular formations aligned with grain boundaries that intersect the surface of Inconel 600, 617, and 625 in ternary NaCl-KCl-MgCl$_2$ molten salt at 700°C after only 100 h of exposure (Sun et al., 2018b). However, neither investigator elaborated on the elemental composition of those features. Again, a review of redox potentials provides some justification for the formation of Ni- and Fe-enriched surface globules. Given the proximity of those features to the suspected initial entry points of attack, a more plausible mechanism hypothesizes that Fe and Ni were dealloyed by the salt. However, given that they have higher redox potentials and accordingly are more thermodynamically favorable to remain in their metallic form compared to Cr in chloride salts, they are redeposited on the surface since accumulating near the originating dealloying site (Guo et al., 2018). Another explanation is proposed from a review of kinetics. The globular formations reported by Ghaznavi et al. were observed in alignment with grain boundaries that intersected with the surface (Ghaznavi et al., 2022b). Potentially, these regions could correlate to grain boundaries that exhibited too high of a surface energy to be favorable for corrosion attack, leaving the surrounding areas depleted of these elements. However, additional studies are needed to further elucidate the mechanism for the formation of the surface globules.

The presence of Mo$_3$Si$_5$ and τ_2 precipitates correlate to precipitate strengthening in Ni-based superalloys. Mo-enriched and carbide (e.g. M$_6$C, M$_{23}$C$_6$, *etc.*) precipitates are commonly integrated into Alloy 617 to enhance mechanical properties (Ren et al., 2010). Intergranular Mo-enriched precipitates were observed in as-received Alloy 617 in this investigation, Supplementary Figure S1. Previous investigations have reported the formation of intergranular Si-Mo-enriched M$_6$C carbides in heat-treated Ni-Mo-Cr superalloys (Xu et al., 2015; Liu et al., 2020). Si has been reported to promote the diffusion of elements and reduce C to form carbides precipitates near grain boundaries (Liu et al., 2020). It is noteworthy to mention that TEM EDS analysis in this investigation did indicate slight C enrichment in the Mo$_3$Si$_5$ (Figure 8) and Cr-enriched precipitates (Supplementary Figure S2), but no conclusive evidence is able to discern elucidation of a corrosion-induced Si-Mo-enriched M$_6$C carbide or Cr-based carbide, respectively. The presence of τ_2 precipitates, a Mn$_{23}$Th$_6$ type structure, would be a novel precipitate to be associated with Alloy 617 (Raghavan, 2005; Ren et al., 2010). Al and Ti are included in Alloy 617 to form Ni$_3$(Al,Ti) (γ') precipitates, which enhance mechanical properties and are thermodynamically stable up to 1,000°C (Klöwer, 2017). In addition, the presence of γ' precipitates have been observed for as long as 100,000 h at 700 °C and has notably been observed to increase in concentration in thermally aged Alloy 617 at 650 and 750°C for up to 5,300 h (Benz and Richardwright, 2013; Klöwer, 2017). The lack of detection of γ' precipitates after thermal aging for 1,000 h and corrosion in NaCl-MgCl$_2$ eutectic salt could indicate that the corrosion mechanism has indirectly induced a phase transformation of γ' to τ_2 precipitates, but additional analysis is required to confirm.

Overall, results of this investigation and assessment of the literature indicate that the proposed mechanism for the corrosion of Alloy 617 by NaCl-$MgCl_2$ eutectic salt is comprised of three main steps, Figure 9: 1) The presence of salt moisture impurities spurs interaction of the Mg, Na, and Cl ions with select grain boundaries at the surface of the alloy. 2) After the initial breach, salt percolates along grain boundaries, O reacting with Cr and establishing a diffusion gradient that initiates Cr dealloying. Fe and Ni are affected by the Cr dealloying, also following the concentration gradient to the Cr-depleted grain and subsequently undergoing intergranular dealloying, further facilitating Cr dissolution. Ni and Fe are less soluble in the salt and phase out of solution to redeposit on the surface, forming globules near the origin point of the corrosion attack. 3) O also reacts with Mg from the salt and dealloyed Al to form $MgAl_2O_4$. Also, Mo_3Si_5 and τ_2 precipitates in the alloy matrix are dissolved by the salt and eventually a heterogeneous porous network forms in regions that have been significantly attacked.

This investigation introduces a novel perspective on the application of multi-modal characterization techniques to elucidate the corrosion mechanism, particularly elemental and microstructural evolution, of MCFR structural material Alloy 617 in NaCl-$MgCl_2$ eutectic salt at 700°C for 1,000 h. The corrosion response of Alloy 617 to the NaCl-$MgCl_2$ eutectic salt exhibited behaviors commonly observed and unlike other Ni-based superalloys. Evidence of intergranular attack, Ni and Fe dealloying, and Cr-O enrichment along the grain boundary observed along with development of insoluble $MgAl_2O_4$ within the porous network. The proposed mechanism involves a feedback loop of intergranular Cr, Ni, Fe, and Mo dealloying, intergranular Cr-O ahead of the corrosion front, dissolving Mo_3Si_5 and τ_2 precipitates embedded in the alloy matrix, and formation of Ni-Fe enriched surface globules resulting from the attack. In addition, precipitates are detected in the alloy bulk and attacked by the salt. Furthermore, the lack of detection of γ' precipitates could indicate that the molten salt corrosion mechanism has indirectly induced a phase transformation of γ’ to τ_2 precipitates. Ultimately, a discontinuous porous network forms from the surface. Based on these results, this investigation demonstrates a comprehensive understanding of molten salt corrosion mechanisms in a complex material system such as a commercial alloy for applications in MCFRs.

Data availability statement

The datasets presented in this study can be found at the United States Department of Energy Office of Scientific and Technical Information database located at https://www.osti.gov/dataexplorer/.

Author contributions

TC-J contributed to conceptualization, data curation, formal analysis, funding acquisition, investigation, methodology, project administration, visualization, and writing of original draft and review/editing of final draft. DM contributed to data curation, formal analysis, investigation, methodology, visualization, validation, and review/editing of final draft. GC contributed to conceptualization, methodology, validation, and review/editing of final draft. LH contributed to conceptualization, funding acquisition, methodology, and review/editing of final draft.

Funding

Work was supported through the INL Laboratory Directed Research and Development Program under DOE Idaho Operations Office Contract DE-AC07-05ID14517, including the completion of the investigation, access to data repository, and publication fees.

Acknowledgments

Special thanks to the operations and radiological control support staff at the INL Irradiated Materials Characterization Laboratory and Electron Microscopy Laboratory.

Conflict of interest

The authors declare that the research was conducted in the absence of any commercial or financial relationships that could be construed as a potential conflict of interest.

The Reviewer DA declared a shared parent affiliation with the author TCJ, DJM, GC at the time of the review.

Publisher’s note

Supplementary material

The Supplementary Material for this article can be found online at: https://www.frontiersin.org/articles/10.3389/fnuen.2022.1049693/full#supplementary-material

References

Bawane, K., Liu, X., Gakhar, R., Woods, M., Ge, M., Xiao, X., et al. (2021). Visualizing time-dependent microstructural and chemical evolution during molten salt corrosion of Ni-20Cr model alloy using correlative quasi *in situ* TEM and *in situ* synchrotron X-ray nanotomography. *Corros. Sci.* 195, 109962. doi:10.1016/j.corsci.2021.109962

Benz, J., and Richardwright, T. L. (2013). Aging of alloy 617 at 650 and 750°C [internet]. Available at: http://www.inl.gov.

Caldwell, A. S., Itskos, G., and Sandhage, K. H. (2021). Air-stable, earth-abundant molten chlorides and corrosion-resistant containment for chemically-robust, high-temperature thermal energy storage for concentrated solar power. *Mat. TodayKidlingt.* 46, 9–17. doi:10.1016/j.mattod.2021.02.015

C. B. Carter and D. B. Williams (Editors) (2016). *Transmission electron microscopy [internet]* (New York, NY: Springer International Publishing).

Ding, W., Shi, H., Jianu, A., Xiu, Y., Bonk, A., Weisenburger, A., et al. (2019). Molten chloride salts for next generation concentrated solar power plants: Mitigation strategies against corrosion of structural materials. *Sol. Energy Mater. Sol. Cells* 193, 298–313. [Internet]. doi:10.1016/j.solmat.2018.12.020

Ding, W., Shi, H., Xiu, Y., Bonk, A., Weisenburger, A., Jianu, A., et al. (2018). Hot corrosion behavior of commercial alloys in thermal energy storage material of molten MgCl2/KCl/NaCl under inert atmosphere. *Sol. Energy Mater. Sol. Cells* 184, 22–30. [Internet]. doi:10.1016/j.solmat.2018.04.025

Ezell, N. D. B., Raiman, S. S., Kurley, J. M., and McDuffee, J. (2020). Neutron irradiation of alloy N and 316L stainless steel in contact with a molten chloride salt. *Nucl. Eng. Technol.* 53, 920–926. [Internet]. doi:10.1016/j.net.2020.07.042

Fukumoto, K. I., Fujimura, R., Yamawaki, M., and Arita, Y. (2015). Corrosion behavior of Hastelloy-N alloys in molten salt fluoride in Ar gas or in air. *J. Nucl. Sci. Technol.* 52 (10), 1323–1327. doi:10.1080/00223131.2015.1043155

Ghaznavi, T., Bryk, M. A., Persaud, S. Y., and Newman, R. C. (2022). Alloying effects in high temperature molten salt corrosion. *Corros. Sci.* 197, 110003. doi:10.1016/j.corsci.2021.110003

Ghaznavi, T., Persaud, S., and Newman, R. C. (2022). Electrochemical corrosion studies in molten chloride salts. *J. Electrochem. Soc.* 169, 061502. [Internet]. doi:10.1149/1945-7111/ac735b

Gill, S. K., Sure, J., Wang, Y., Layne, B., He, L., Mahurin, S., et al. (2021). Investigating corrosion behavior of Ni and Ni-20Cr in molten ZnCl2. *Corros. Sci.* 179, 109105. doi:10.1016/j.corsci.2020.109105

Goldstein, J. I., Newbury, D. E., Michael, J. R., Ritchie, N. W. M., Scott, J. H. J., and Joy, D. C. (2018). *Scanning electron microscopy and X-ray microanalysis [internet]*. New York, NY: Springer New York.

Gomez-Vidal, J. C., and Tirawat, R. (2016). Corrosion of alloys in a chloride molten salt (NaCl-LiCl) for solar thermal technologies. *Sol. Energy Mater. Sol. Cells* 157, 234–244. doi:10.1016/j.solmat.2016.05.052

Grégoire, B., Oskay, C., Meißner, T. M., and Galetz, M. C. (2020). Corrosion mechanisms of ferritic-martensitic P91 steel and inconel 600 nickel-based alloy in molten chlorides. Part II: NaCl-KCl-MgCl2 ternary system. *Sol. Energy Mater. Sol. Cells* 216, 110675. doi:10.1016/j.solmat.2020.110675

Guo, S., Zhang, J., Wu, W., and Zhou, W. (2018). Corrosion in the molten fluoride and chloride salts and materials development for nuclear applications. *Prog. Mat. Sci.* 97, 448–487. doi:10.1016/j.pmatsci.2018.05.003

Guo, S., Zhuo, W., Wang, Y., and Zhang, J. (2020). Europium induced alloy corrosion and cracking in molten chloride media for nuclear applications. *Corros. Sci.* 2020, 163. doi:10.1016/j.corsci.2019.108279

Huneau, B., Rogl, P., Zeng, K., Schmid-Fetzer, R., Bohn, M., Bauer, J., et al. (1999). The ternary system Al-Ni-Ti Part I: Isothermal section at 900°C; Experimental investigation and thermodynamic calculation. *Intermetallics* 7 (12), 1337–1345. (Barking) [Internet]. doi:10.1016/s0966-9795(99)00054-0

Indacochea, J. E., Smith, J. L., Litko, K. R., Karell, E. J., and Raraz, A. G. (2001). High-Temperature oxidation and corrosion of structural materials in molten chlorides. *Oxid. Metals* 55 (1–2), 1–16. doi:10.1023/a:1010333407304

Jagadeeswara Rao, C., and Ningshen, S. (2020). High temperature molten salt corrosion of structural materials in UCl3–LiCl–KCl. *Corros. Eng. Sci. Technol.* 55 (5), 425–433. [Internet]. doi:10.1080/1478422X.2020.1741869

Jalbuena, A. A., Ury, N., Bae, J., Faraj, C., Hanan, K., Kasnakjian, S., et al. (2019). Corrosion of Al 0.1 CoCrFeNi high entropy alloy in a molten eutectic salt. *J. Electrochem. Soc.* 166 (11), C3488–C3492. doi:10.1149/2.0561911jes

Keny, S. J., Gupta, V. K., Kumbhar, A. G., and Rangarajan, S. (2019). Corrosion tests of various alloys in fluorides of lithium, sodium and potassium (FLiNaK) medium for molten salt reactors in the temperature range of 550-750°c using electrochemical techniques. *Indian J. Chem. Technol.* 26 (1), 84–88. doi:10.56042/ijct.v26i1.13027

Klöwer, J. (2017). "Alloy 617 and derivatives," in *Materials for ultra-supercritical and advanced ultra-supercritical power plants* (Amsterdam, Netherlands: Elsevier), 547–570.

Knosalla, C., Lau, M., Schmies, L., Lippmann, W., and Hurtado, A. (2020). Investigation on the corrosion behavior of nickel-base alloys in molten chlorides for sensible heat energy applications. *Adv. Eng. Mat.* 22 (7), 2000099. doi:10.1002/adem.202000099

Koger, J. W. (1974). "Chromium depletion and void formation in Fe—Ni—Cr alloys during molten salt corrosion and related processes," in *Advances in corrosion science and Technology [internet]* (Boston, MA: Springer US), 245–318.

Lei, Q., Zhang, X., Gao, M., Wen, W., Jia, Y., Liu, H., et al. (2021). Inconel 617 corrosion in FLiNaK molten salts: An *in situ* X-ray diffraction study. *Corros. Sci.* 182, 109289. doi:10.1016/j.corsci.2021.109289

Limiting Compositions of Alloy (2019). Nominal or limiting compositions of alloy. In: *Structural alloys for nuclear energy applications*. Amsterdam, Netherlands: Elsevier.

Liu, B., Wei, X., Wang, W., Lu, J., and Ding, J. (2017). Corrosion behavior of Ni-based alloys in molten NaCl-CaCl2-MgCl2 eutectic salt for concentrating solar power. *Sol. Energy Mater. Sol. Cells* 170, 77–86. [Internet]. doi:10.1016/j.solmat.2017.05.050

Liu, T., Yang, M., Han, F., and Dong, J. (2020). Influence mechanism of silicon on carbide phase precipitation of a corrosion resistance nickel based superalloy. *Materials* 13 (4), 959. doi:10.3390/ma13040959

Olson, L. C., Ambrosek, J. W., Sridharan, K., Anderson, M. H., and Allen, T. R. (2009). Materials corrosion in molten LiF-NaF-KF salt. *J. Fluor. Chem.* 130 (1), 67–73. doi:10.1016/j.jfluchem.2008.05.008

Patel, K., Sadeghilaridjani, M., Pole, M., and Mukherjee, S. (2021). Hot corrosion behavior of refractory high entropy alloys in molten chloride salt for concentrating solar power systems. *Sol. Energy Mater. Sol. Cells* 230, 111222. [Internet]. doi:10.1016/j.solmat.2021.111222

Pragnya, P., Gall, D., and Hull, R. (2021). *In situ* transmission electron microscopy of high-temperature inconel-625 corrosion by molten chloride salts. *J. Electrochem. Soc.* 168 (5), 051507. doi:10.1149/1945-7111/ac0225

Raghavan, V. (2005). Al-Ni-Ti (Aluminum-Nickel-Titanium). *J. Phase Equilibria Diffus.* 26 (3), 268–272. doi:10.1361/15477030523652

Ren, W., Swindeman, R. W., Swindeman, R. W., and Santella, M. L.(2010). Developing a nuclear grade of alloy 617 for gen IV nuclear energy systems [Internet]. Available at: https://www.researchgate.net/publication/349412451.

Salinas-Solano, G., Porcayo-Calderon, J., Gonzalez-Rodriguez, J. G., Salinas-Bravo, V. M., Ascencio-Gutierrez, J. A., and Martinez-Gomez, L. (2014). High temperature corrosion of inconel 600 in NaCl-KCl molten salts. *Adv. Mater. Sci. Eng.* 2014, 1–8. doi:10.1155/2014/696081

Shankar, A. R., Thyagarajan, K., and Mudali, U. K. (2013). Corrosion behavior of candidate materials in molten LiCl-KCl salt under argon atmosphere. *Corros. [Internet]* 69 (7), 655–665. doi:10.5006/0746

Sun, H., Wang, J., Li, Z., Zhang, P., and Su, X. (2018). Corrosion behavior of 316SS and Ni-based alloys in a ternary NaCl-KCl-MgCl2 molten salt. *Sol. Energy* 171, 320–329. doi:10.1016/j.solener.2018.06.094

Sun, H., Zhang, P., and Wang, J. (2018). Effects of alloying elements on the corrosion behavior of Ni-based alloys in molten NaCl-KCl-MgCl2 salt at different temperatures. *Corros. Sci.* 143, 187–199. doi:10.1016/j.corsci.2018.08.021

Vignarooban, K., Pugazhendhi, P., Tucker, C., Gervasio, D., and Kannan, A. M. (2014). Corrosion resistance of Hastelloys in molten metal-chloride heat-transfer fluids for concentrating solar power applications. *Sol. Energy* 103, 62–69. [Internet]. doi:10.1016/j.solener.2014.02.002

Wang, B., Huang, J., Fan, J., Dou, Y., Zhu, H., and Wang, D. (2017). Preparation of FeCoNiCrMn high entropy alloy by electrochemical reduction of solid oxides in molten salt and its corrosion behavior in aqueous solution. *J. Electrochem. Soc.* 164 (14), E575–E579. doi:10.1149/2.1521714jes

Xu, Z., Jiang, L., Dong, J., Li, Z., and Zhou, X. (2015). The effect of silicon on precipitation and decomposition behaviors of M6C carbide in a Ni-Mo-Cr superalloy. *J. Alloys Compd.* 620, 197–203. doi:10.1016/j.jallcom.2014.09.112

Yang, T., Su, Y., Liu, H., Dai, Z., Liang, X., and Wu, X. (2020). Corrosion behavior of Inconel 625 deposited metal in molten KCl-MgCl2. *Mat. Res. Express* 7 (12), 126505. doi:10.1088/2053-1591/abcdd9

Yang, X., Zhang, D., Liu, M., Feng, S., Xue, W., Liu, H., et al. (2016). Corrosion of SiC induced by Hastelloy N alloy and its corrosion products in LiF-NaF-KF molten salt. *Corros. Sci.* 109, 62–67. doi:10.1016/j.corsci.2016.03.029

Ye, X. X., Ai, H., Guo, Z., Huang, H., Jiang, L., Wang, J., et al. (2016). The high-temperature corrosion of Hastelloy N alloy (UNS N10003) in molten fluoride salts analysed by STXM, XAS, XRD, SEM, EPMA, TEM/EDS. *Corros. Sci.* 106, 249–259. doi:10.1016/j.corsci.2016.02.010

Yu, W., Singh, D., and France, D. M. (2019). Investigation of corrosion of 304 stainless, inconel 625, and haynes 230 in a chloride-salt-based thermal storage medium. *J. Mat. Eng. Perform.* 28 (12), 7379–7389. doi:10.1007/s11665-019-04508-y

Zhu, M., Ma, H., Wang, M., Wang, Z., and Sharif, A. (2016). Effects of cations on corrosion of inconel 625 in molten chloride salts. *High Temp. Mater. Process.* 35 (4), 337–345. doi:10.1515/htmp-2014-0225